Recent Developments in Microtomography at GeoSoilEnviroCARS

Mark L. Rivers and Yanbin Wang

Department of Geophysical Sciences and Center for Advanced Radiation Sources, University of Chicago, 9700 South Cass Avenue., Argonne, IL 60439

ABSTRACT

A facility for x-ray computed microtomography (CMT) is operating as a national user facility for earth and environmental sciences research on the bending magnet beamline at the GeoSoilEnviroCARS sector at the Advanced Photon Source (APS). The APS bending magnet has a critical energy of 20 keV, and thus provides high flux at photon energies up to 100 keV, making it well suited to imaging a wide range of earth materials up to several cm in size. The beamline is equipped with a Si (111) double-crystal monochromator covering the energy range from 5 to 70 keV with beam sizes up to 50mm wide and 6mm high. The transmitted x-rays are imaged with a single crystal YAG or $CdWO_4$ scintillator, a microscope objective and a 1300x1030 pixel 12-bit 5MHz CCD detector. The maximum spatial resolution is under 1.5 μm in both the transmission radiographs and the reconstructed slices. Data collection times for full 3-D datasets range from 5-60 minutes. This facility has been used for a wide range of studies, including multiphase fluids in porous media, high-pressure studies, meteorites, and hyper-accumulating plants. We present recent technical improvements in the system, which include improved optics for samples larger than 5mm, significant reduction of ring artifacts, and correction of mechanical errors in the rotation stage.

Keywords: Tomography, microtomography, geosciences.

1. INTRODUCTION

X-ray computed microtomography (CMT) has great potential for application to research problems in geosciences. It provides the ability to examine the internal structure of objects which cannot be sectioned, either because the objects are too valuable (e.g. some meteorites and fossils), because the objects are too fragile to be sectioned (e.g. interplanetary dust particles and soil aggregates), or simply because physical sectioning is too time consuming. Synchrotron radiation makes it possible to extend the CT technique to micron spatial resolution with reasonable data acquisition times. GeoSoilEnviroCARS (GSECARS) is a national user facility for earth and environmental sciences research at sector 13 at the Advanced Photon Source at Argonne National Laboratory. This facility provides users with techniques including CMT, high-pressure diffraction in the diamond anvil cell and multi-anvil press, x-ray fluorescence microprobe, microspectroscopy, and surface and microcrystal diffraction. This paper is intended to summarize the technical improvements and new capabilities since our previous reports[1,2].

2. EXPERIMENTAL

2.1 X-ray source

In this paper we discuss only our absorption CT system, which runs on the APS bending magnet, station 13-BM-D. We also operate an x-ray microprobe facility on our undulator beamline in station 13-ID-C. This station is used for trace-element fluorescence microtomography experiments, which are beyond the scope of this paper. The 13-BM-D CMT facility runs about 25% of the time in this station, which is also used for high-pressure and EXAFS experiments.

The APS bending magnet source has a critical energy of 20 keV, and thus provides high flux at photon energies up to 100 keV, making it well suited to imaging a wide range of earth materials up to several cm in size. The GSECARS bending magnet beamline provides a 2.5 mrad fan of radiation, permitting in principal studies of objects up to 125 mm in diameter in the experimental station 50 m from the source. The vertical beam size is about 5 mm maximum, due to the narrow opening angle of the synchrotron radiation. The beamline is equipped with a Si (111) fixed-offset double-crystal monochromator, covering the range 5-70 keV. This monochromator can be removed for white beam studies when required. An ion chamber just upstream of the CMT apparatus is used in a feedback system to stabilize the second crystal of the monochromator. The beamline is also equipped with a 1 meter long bent-flat vertical mirror. This mirror

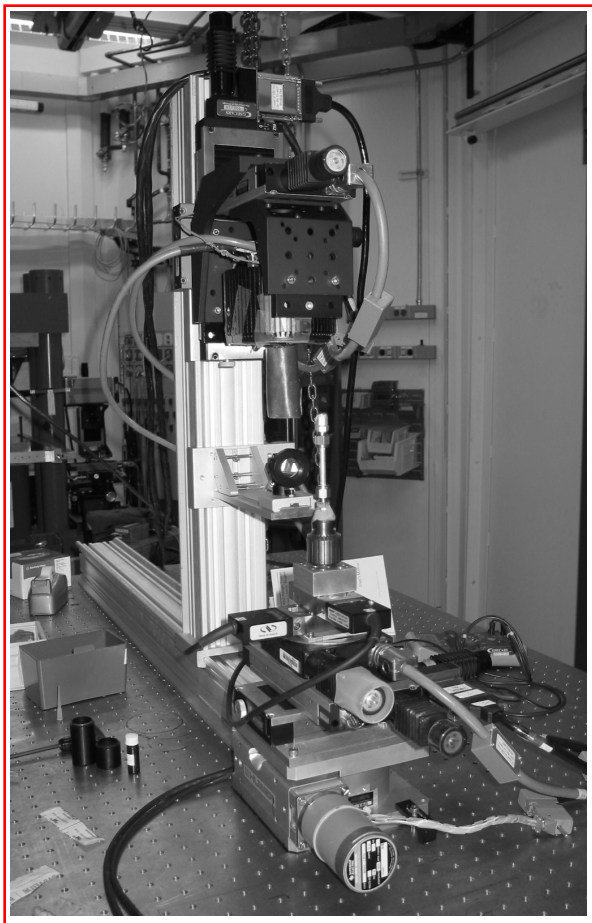

Figure 1. Photograph of the absorption CT apparatus in station 13-BM-D. The x-ray bean enters from the right, and passes through the sample, to the scintillator screen. The microscope objective and CCD camera are mounted on a vertical translation stage,

can be used to focus or defocus the beam, and can be used either with monochromatic or white beam. We have not yet used this mirror for microtomography experiments, but it has been used to provide a larger vertical beam size (by defocusing) and to provide a large bandwidth pink beam for very fast data acquisition during high-speed radiography experiments[3].

2.2 CMT setup

Figure 1 is a photograph of the CMT setup in the 13-BM-D station. The first component is a sample stage with 5 degrees of freedom, followed by a single-crystal YAG or $CdWO_4$ scintillator that converts the transmitted x-rays to visible light. The scintillator is imaged with a microscope objective (5X to 20X) and a variable tube length to match the field of view to the sample size. A Nikon macro lens, discussed in the next section, has recently been added for use with samples 5mm and larger. Using these optics the field of view can be adjusted between <1 mm to >20 mm. The image is projected onto a Roper Scientific MicroMAX 5MHz 5MHz CCD detector. This camera has a 8.7x6.9mm CCD chip with 6.7x6.7 μm pixels. The distance from the sample to the scintillator can be adjusted by translating the vertical post in Figure 1, from 20mm to 800mm. Adjusting this distance controls the amount of phase contrast versus absorption contrast in the images.

3. TECHNICAL IMPROVEMENTS

3.1 Optics

The tomography apparatus at GSECARS is often used for studies of relatively large objects, up to 1cm in horizontal width. The synchrotron is very useful for such studies in spite of the relatively large pixel sizes (10-20 μm) because of the tunable energies. For example, many studies use differential absorption tomography above and below the I and Cs edges to image the location of aqueous and organic fluids in porous media[4,5,6] . In the past we have used a Mitutoyu M Plan Apo 5 (5X) long working distance objective for such large fields of view. Using tube lengths between 0 and 12.5mm produces fields of view between 11.1 and 8.1 mm. This corresponds to pixel sizes on the sample ranging from 8.5 μm (17 μm with 2x2 binning) to 6.2 μm (12.4 μm with binning). The lens was obviously being used far from its design magnification, since it was being used for magnifications of 0.8 to 1.1, rather than 5X.

We have recently purchased a Nikon AF Micro Nikkor 60mm macro lens to be used for these large fields of view. This lens produces significantly sharper images, and requires shorter exposure times. When this lens is at its closest focus with no tube extender it produces an 8.7x6.9 mm field of view on the MicroMAX CCD. With a 50mm tube extender the field of view is decreased to 4.4x3.5 mm. By focusing the lens at a larger distance the field of view can be increased to very large values. We have used up to 20mm horizontal fields of view with this lens.

Figure 2 compares the reconstructed slices through a column containing sand and water collected at 33.269 keV with the Mitutoyu 5X objective and the Nikon macro lens. The field of view is 7.2x5.7 mm, and the pixel size is 11.1 μm. The Nikon macro lens is clearly producing much sharper images. Figure 3 compares vertical sections through a meteorite data set collected at 38 keV with the same field of view. Again, the Nikon macro lens is producing far sharper images. For the data in Figure 3 the exposure time per frame with the Mitutoyu 5X objective was 0.65 seconds, compared to 0.35 seconds for the Nikon macro lens for the same counts on the CCD. Thus, the Nikon lens requires only 53% of the exposure time of the Mitutoyu lens, significantly reducing data collection time while improving image quality.

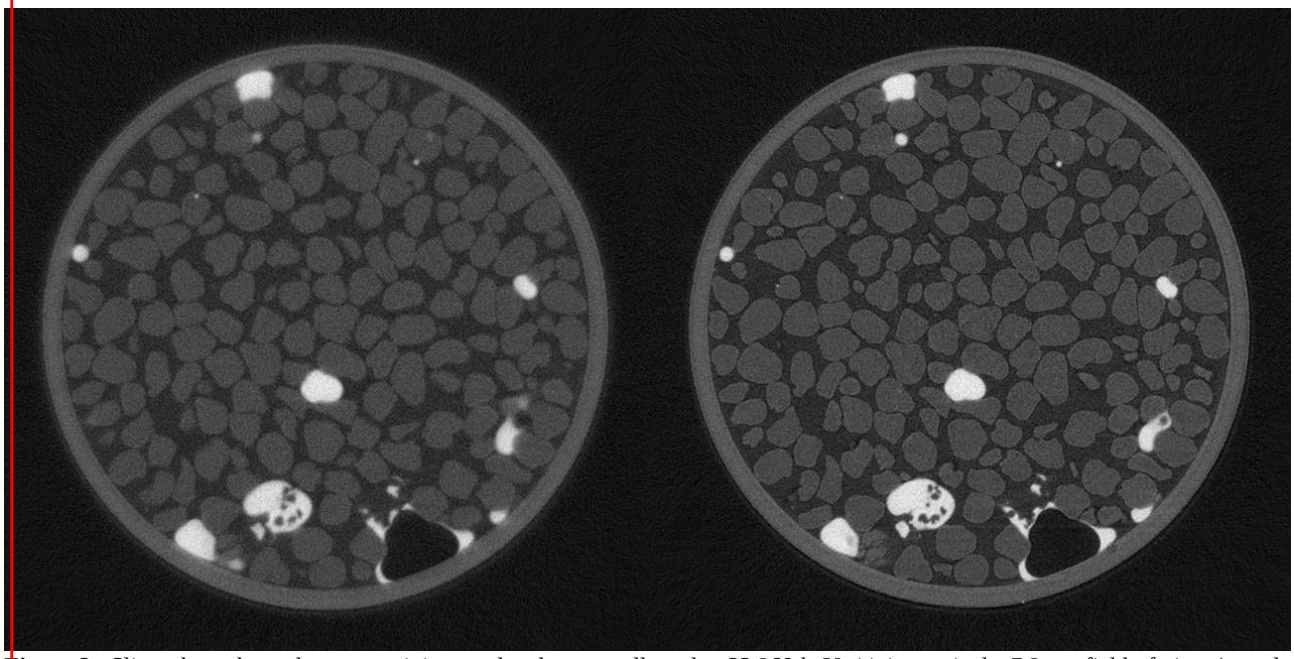

Figure 2. Slices through a column containing sand and water collected at 33.269 keV, 11.1 µm pixels, 7.2mm field of view (sample GS_A15). A (left): Mitutoyu 5X long-working distance objective with 17.5mm tube; B (right): Nikon macro lens with PK-11A extender tube.

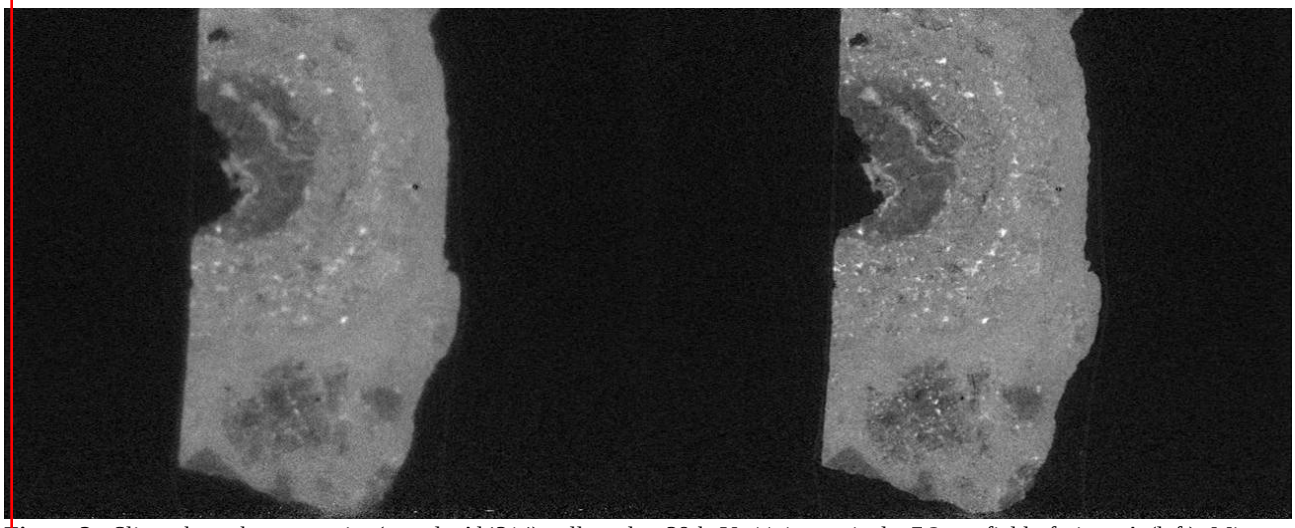

Figure 3. Slices through a meteorite (sample Al4314) collected at 38 keV, 11.1 µm pixels, 7.2mm field of view. A (left): Mitutoyu 5X long-working distance objective with 17.5mm tube; B (right): Nikon macro lens with PK-11A extender tube.

3.2 Data Collection and Scintillators

Our data collection software has been previously described[1,2]. A major recent improvement is that it is now possible to collect a single file containing all of the projections, which reduces the software overhead to a negligible level, so that the collection time is controlled by the exposure time, and time required to move the motors. We often collect data sets in which the CCD is binned 2x2, for an effective resolution of 650x515. This reduces the data collection time by a factor of 8 relative to unbinned data (factor of 4 due to binning of CCD, and another factor of 2 because 2X fewer angles are required). It also reduces the data storage and processing requirements by this amount, but most importantly allows users to collect data on 8 times more samples in a given amount of beam time.

Exposure times per projection vary from less than 0.25 seconds for binned data with 10 μm pixels at 30 keV, to more than 10 seconds for unbinned data with 2 μm pixels at 10 keV. We normally collect for times long enough to reach 80-90% of saturation of the 12-bit CCD during the flat field images. These exposure times have been reduced recently through the use of the Nikon macro lens discussed above. We have also found YAG scintillators that are up to 3 times brighter than those that had used in the past. These have essentially identical light output to some new highly polished $CdWO_4$ scintillators that we have obtained from Hilger Crystals in the UK, through Newport in the USA. The $CdWO_4$ should have a shorter x-ray absorption length and hence less depth of field blurring than the YAG crystal at high energy, but we have not yet had a chance to make a quantitative comparison of resolution as a function of energy.

3.3 Data Processing Speed

The data processing is done on a Dell Precision 470 workstation with dual 3.4 GHz Intel Xeon processors and 8GB of RAM. The operating system is the 64-bit version of Redhat Fedora Core 3. We are currently running the 64-bit version of IDL V6.2. The data processing consists of several steps: 1) preprocessing 2) sinogram creation 3) reconstruction 4) visualization and 5) quantification. We use software that we have written in IDL for steps 1, 2 and 4, and that has been previously described[1,2]. The preprocessing step consists of reading all raw data images, correcting for dark current, flat fields, and zingers (direct x-ray hits on the CCD) and outputting the normalized preprocessed data as a single 3-D netCDF volume file. The reconstruction step consists of reading the normalized preprocessed file, and for each slice computing the sinogram, ring artifact reduction (see below), reconstructing, and outputting the reconstructed data as a single 3-D netCDF volume file Reconstruction is done with the FFT-based Gridrec software from Brookhaven[7], but modified to be called from IDL. Gridrec reconstructions appear to be essential identical to those done with filtered backprojection using the IDL Riemann function, with only the details of the noise being significantly different. Gridrec is approximately 15 times faster than filtered backprojection. We have recently enhanced the speed of Gridrec by replacing the Numerical Recipes FFT functions it was using with those from the FFTW package[8]. This resulted in a factor of 3-4 speed improvement with reconstructions that differ only at the level of the machine precision. With this system we can preprocess and reconstruct complete 3-D datasets "in-memory". This is very convenient for visualization, which is handled in IDL.

Table 1 shows the times for preprocessing and reconstruction for typical dataset sizes. For 2x2 binned data from our detector with 720 projections (0.25° steps) the preprocessing time for the entire dataset is 30 seconds, and the reconstruction time is 170 seconds. For unbinned data with 900 projections (0.20° steps) the reconstruction time is 1030 seconds (17 minutes), which is less than the typical time to collect such a data set.

Table 1. Data Processing Times

# columns	# slices	# projections	Preprocessing time for volume (s)	Sinogram time per slice (s)	Reconstruction time per slice (s)	Sinogram and reconstruction time for volume (s)
650	515	720	30	0.11	0.19	170
1024	1024	720	105	0.17	0.58	774
1300	1030	900	200	0.25	0.62	1030

For quantification many users make use of the Blob3D program[9] from R. A. Ketcham at the University of Texas at Austin. Other users employ the 3DMA program[10] from W.B. Lindquist at Stony Brook University. The data processing software we have written is freely available at **http://cars.uchicago.edu/software/idl/tomography.html**

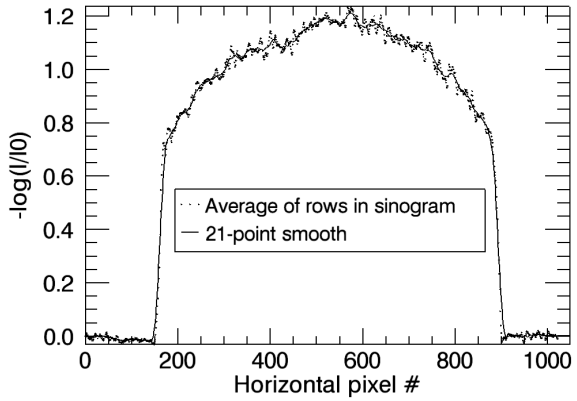

Figure 4. Plot of the average of all rows in the sinogram of slice 512 from an aluminum corrosion test sample. Also plotted is a 21-point smoothed version of the average. The difference between the unsmoothed and smoothed version is use to correct the response of each pixel to reduce ring artifacts.

3.4 Ring Artifacts

Tomography data collected with 1D or 2D detectors such as CCDs is subject to ring artifacts. The root cause of such artifacts is a difference in sensitivity of a pixel or group of pixels relative to neighboring pixels. To first approximation the difference in sensitivity should be removed by normalization to the flat field with no sample present. However, residual differences in sensitivity often remain after flat field corrections. These differences can be due to non-linearity in detector response, since the flat field is typically only collected for a single exposure level, which is higher than that when the sample is present. The differences can also be caused by defects such as scratches in the scintillator which allow light generated in one part of the scintillator to escape and be detected in another location. Other effects can include detector drift with time, or with synchrotron sources, defects in the monochromator changing the harmonic content of some pixels relative to others. Ring artifacts can be eliminated by hardware methods such as time-delay integration[11], but such techniques are difficult to implement for many CCD cameras, and can introduce their own set of problems.

We have implemented a technique for reducing ring artifacts that employs the fact that the average row of the sinogram (averaging over all projection angles) should be a smooth function with little high-frequency content. High-frequency content, i.e. intensity changes over just a few horizontal pixels, are due to undesired sensitivity variations in the system response. These show up as vertical stripes in the sinogram, and as 180° rings in the reconstructed slice. We correct for these variations by computing the "error" for each pixel, defined as the observed average row in the sinogram minus a smoothed version of the average row. The smoothing is done with a boxcar filter with user-selectable width, 9 points being the default. The error for each pixel is then subtracted from that pixel in all rows (projections) in the sinogram. We use subtraction, rather than multiplication, because we are performing the correction after taking the logarithm when computing the sinogram. This is thus the same as correcting by the ratio of the measured to smoothed average row if the correction is done before the logarithm is taken, as is done by Ketcham[12].

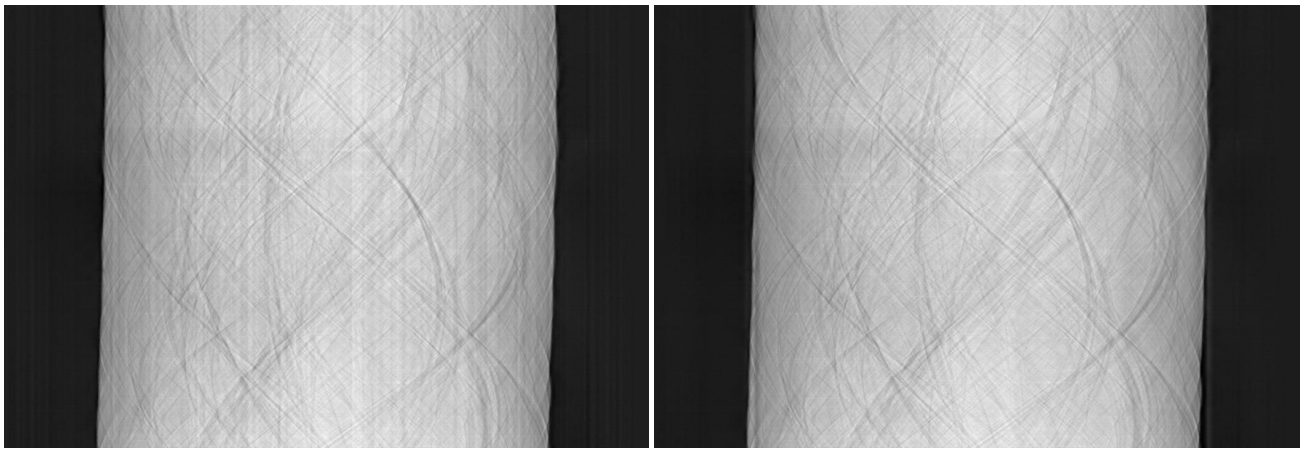

Figure 5. Sinograms of slice 512 from an aluminum corrosion test sample. A (left): before applying correction from 21-point smooth; B (right): after applying correction.

Figure 5A shows the measured sinogram of an aluminum corrosion test sample. Note the vertical stripes in the image. Figure 4 shows the measured average row of this sinogram, and the 21-point smoothed version of this average row.

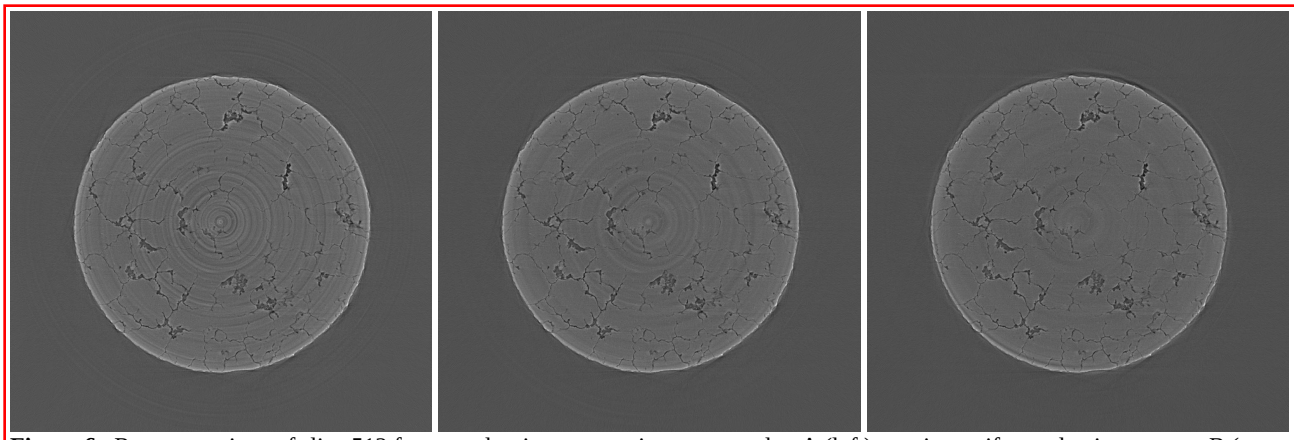

Figure 6. Reconstructions of slice 512 from an aluminum corrosion test sample. A (left): no ring artifact reduction; center: B (center) 9 point smooth of average row of sinogram; C (right): 21-point smooth.

Figure 5B shows the sinogram after correction by the technique described above. Note that the vertical stripes have been significantly reduced in amplitude, particularly the high-frequency components. Figure 6 shows the reconstructions of this sinogram with no ring artifact reduction, and with the above algorithm using 9 point and 21 point smoothing. The technique significantly reduces the ring artifacts, with the 21 point smoothing removing them almost completely.

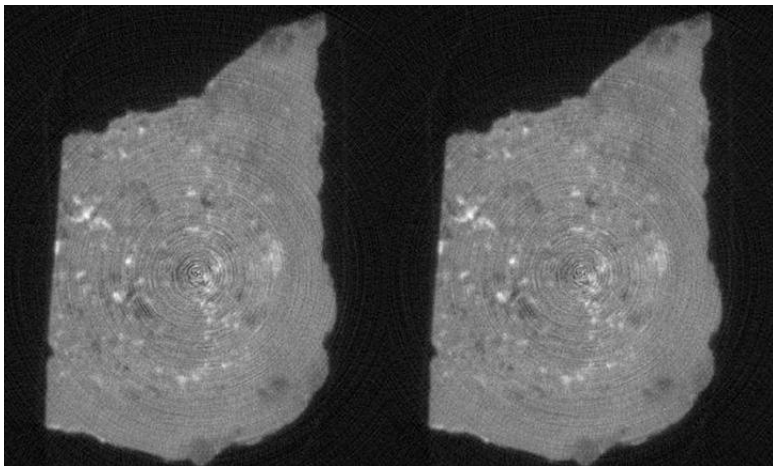

Figure 7. Reconstructions of slice from a meteorite sample. A (left): interpolated flat fields, no ring artifact reduction; B (right): interpolated flat fields, 9-point ring artifact reduction

The only time we see a significant problem with this technique is when imaging cylindrical objects that are close to being centered on the rotation axis. In this case the edge of the cylinder will appear as vertical stripes in the sinogram, and the method will attempt to eliminate them. This can lead to blurring and streaking of the edges of the cylinder. One solution to this problem is to deliberately offset such cylindrical objects from the rotation axis when imaging them.

In spite of the default application of this ring artifact removal technique to data processing at our facility, we noticed that much of our data still contained significant ring artifacts (e.g. Figure 7B). On detailed investigation we discovered that the cause of this was actually noise in the flatfield images that were being used to normalize the data. We normally collect a flat field before the first projection and after the last projection, and at increments of every 50 or 100 projections during data collection. The flat fields are collected as a function of time to correct for changes in the flat fields due to drifts in the incident beam profile, etc. The correction was done by interpolating the flat fields images, so that if a projection N was collected between flat fields A and B then it was normalized using a weighted average of A and B, the weighting being determined by the time the projection was collected relative to the times when the flat fields were collected. While this method is sound in principle, we have discovered that it was contributing significantly to the ring artifacts. Figure 7 shows reconstructed slices of a meteorite sample processed with this technique of flat field interpolation without ring artifact reduction (7A), and with 9-point ring artifact reduction (7B). The rings are very noticeable even with the artifact reduction algorithm.

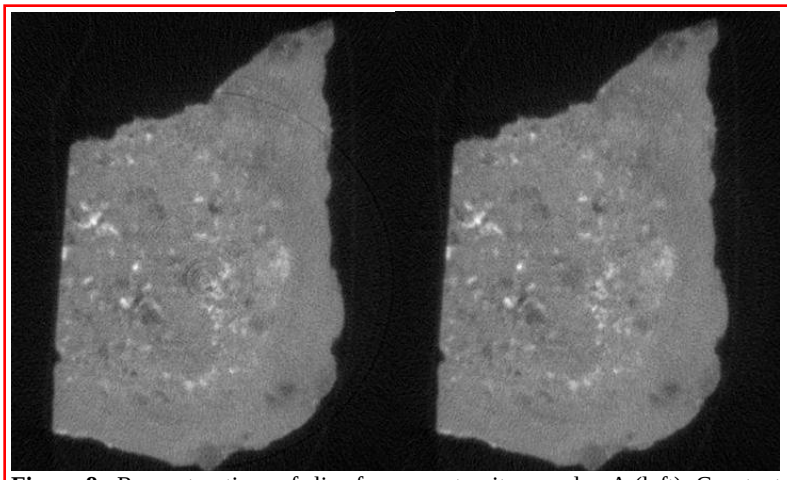

Figure 8. Reconstructions of slice from a meteorite sample. A (left): Constant flat field of 4000 counts, no ring artifact reduction; B (right): Constant flat field of 4000 counts, 9-point ring artifact reduction

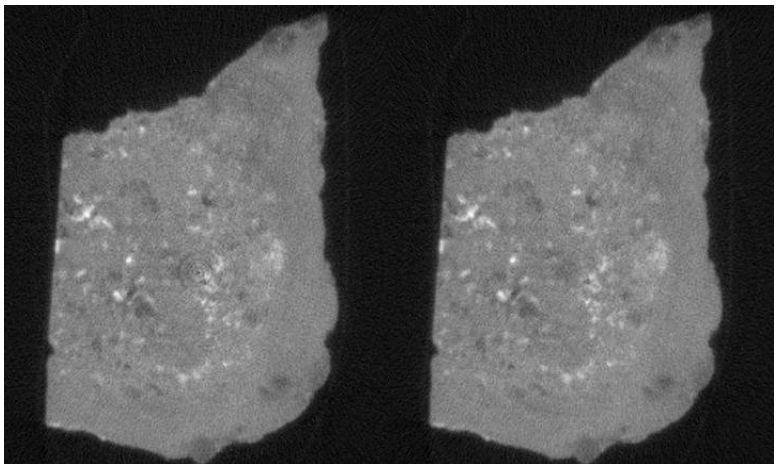

Figure 9. Reconstructions of slice from a meteorite sample. A (left): averaged flat fields, no ring artifact reduction; B (right): averaged flat fields, 9-point ring artifact reduction

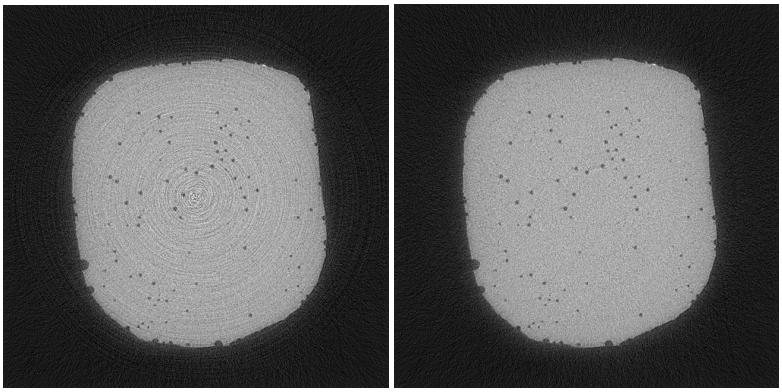

Figure 10. Reconstructions of slice from a glass sample with bubbles. A (left): interpolated flat fields, 9-point ring artifact reduction; B (right): averaged flat fields, 9-point ring artifact reduction.

To demonstrate that nearly all of the rings in Figure 7 are coming from the flat fields we performed another reconstruction shown in Figure 8. In processing the data for Figure 8 we did not use the measured flat field images at all, we simply assumed a constant flat field image of 4000 counts, which corresponds to nearly the full range of our 12-bit CCD. To our surprise this reconstruction is much better than the one using the measured flat fields! Figure 8A shows some minor ring artifacts, but these are almost completely removed by the ring artifact reduction algorithm in Figure 8B. This analysis proves that the ring artifacts in Figure 7 are almost completely due to noise in the flat field images. Because an anomalous pixel value in the flat field is used for many projections, it is amplified and results in much more significant rings than similar noise in a single projection. The technique we were using of interpolating the flat fields was generating serious ring artifacts because we were doing nothing to suppress the noise in the flat field images. Furthermore, because we were interpolating the flat fields, each flat field was only used for a limited range of angles, typically between 12 and 25 degrees. This meant that the pixel anomalies in the flat fields were only projected over a limited angular range in the reconstruction. In other words the rings do not cover 180° but only 12°-25°. The limited angular range of the rings caused by interpolating the flat fields makes the ring artifact reduction algorithm very ineffective, since it applies corrections to all 180° of the sinogram.

A solution to the problem is not to interpolate the flat fields, but rather to simply average them and use the average flat field for all projections. This reduces the noise in the flat fields, and hence the ring artifacts. Figure 9 shows the result when the actual flat field data are used for normalization, but using averaging rather than interpolation. There are some minor ring artifacts in Figure 9A, but these are almost completely removed by the algorithm described above because the rings cover the full 180° of the sinogram (Figure 9B). By averaging rather than interpolating flat fields were are able to reprocess data already collected and significantly reduce the ring artifacts Figure 10 shows the difference

between using interpolated flat fields and average flat fields for another sample, a glass containing bubbles.

The disadvantage of averaging flat fields is that any temporal variable in the flat fields is lost, and it is not possible to correct for drift in the incident beam profile. In the future we will modify our data collection software to measure multiple flat fields when we were previously collecting a single flat field, i.e. periodically during data collection. We will then average the flat fields collected at the same projection angle for noise reduction, and then interpolate these averages as a function of time to correct for drift.

3.5 Rotation stage errors

Accurate tomography data requires that the mechanical errors in the rotation stage be small compared with the pixel size. These errors include rotation angle error, radial runout (eccentricity), axial runout, and wobble. As microtomography pushes the spatial resolution to the micron level and below, the mechanical precision of the stage becomes increasingly problematic. We have found that some of the stages (Newport URM-80) we have been using for microtomography have significant errors at the few micron level, probably due to wear. We have developed an algorithm to partially correct our data for these mechanical errors. While we have now replaced these stages with newer ones having errors less than a micron, we believe this algorithm may prove useful in nano-tomography applications where rotation stages errors may always be larger than the pixel size, or in specialized applications such as existing stages inside SEM instruments[13]. It is also very useful for reprocessing existing data collected with the poorer stages.

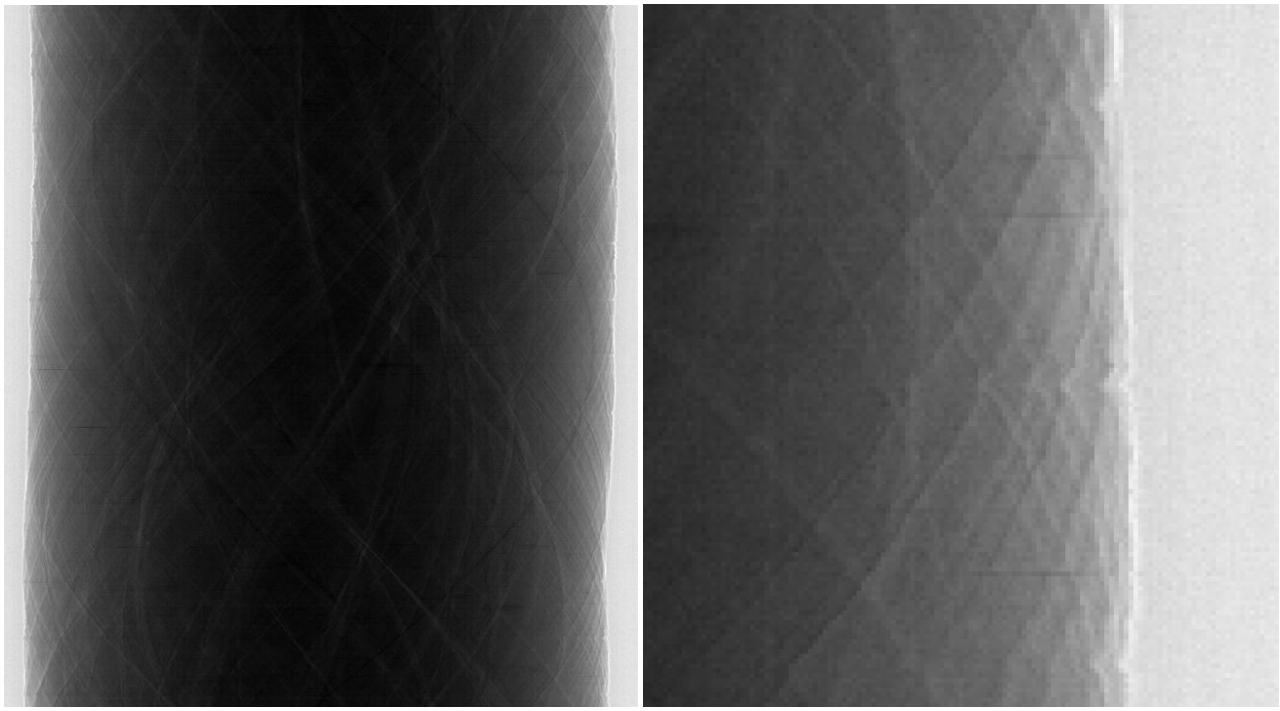

Figure 11. Sinogram from sandstone sample with 3.36 μm pixels. A (left): sinogram over 180° of slice 236; B (right): enlargement of lower right part of sinogram. Note the ragged nature of the edge of the object at some angles, due to imperfections in the rotation stage.

Figure 11 shows the sinogram of a sandstone collected with 3.36 μm pixel size. In Figure 11B one can clearly see from the ragged right edge that some projections have been shifted horizontally relative to their correct locations. This is due to mechanical imperfections in the rotation stage. To implement an algorithm to correct the sinogram for such errors we first note that if we compute the center-of-gravity of each row in the sinogram, the center of gravity itself must describe a sine wave as a function of projection angle. Figure 12 shows the measured center of gravity for the sinogram shown in Figure 11, as well as the best fit sine function. Figure 13 shows the difference between the measured and fitted curves. This difference has three main components: 1) noise due to measurement error; 2) any systematic errors due to non-

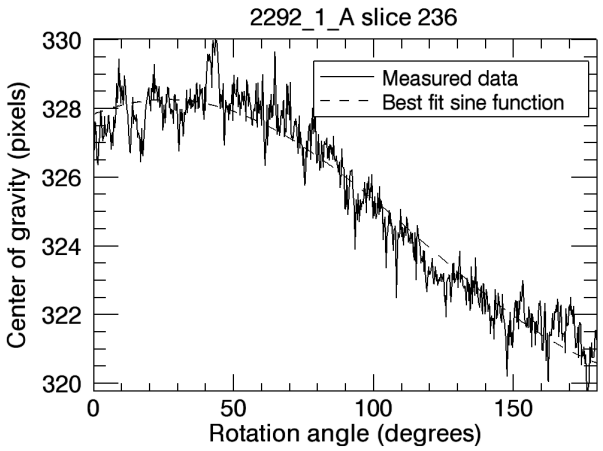

Figure 12. Center-of-gravity of sinogram and best-fit sine function.

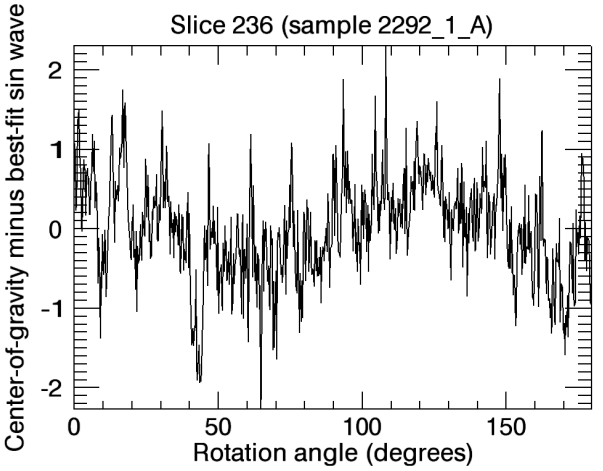

Figure 13. Deviation of center-of-gravity of sinogram from best-fit sine function.

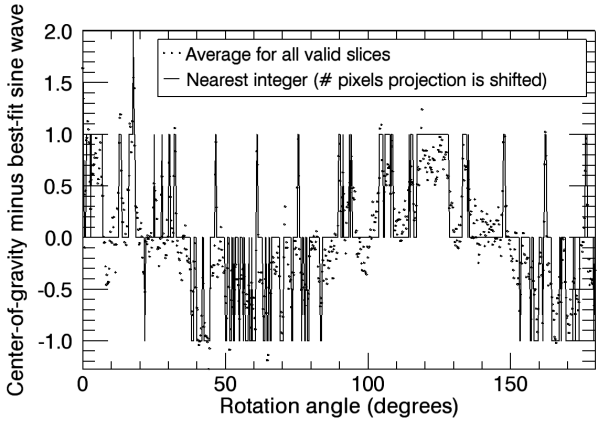

Figure 15. Average deviation of center-of-gravity of sinogram from best-fit sine function for all valid slices. Also plotted is the nearest integer to the average, which is the number of pixels that each projection in the sinogram is shifted to correct the data.

linearities in the measurement system which invalidate the assumption that the integral of I/I0 is conserved as a function of rotation angle; 3) contributions from the mechanical errors in the rotation stage.

The dominant errors in the rotation stage will cause translation of the sample perpendicular to the rotation axis (horizontal), i.e. we can ignore tilting of the sample and translation errors parallel to the (vertical) rotation axis. In this case the errors introduced by the rotation stage will be the same for every slice, and we can reduce the noise in estimating the rotation stage errors by averaging over all of the slices. Figure 14 shows the deviation of the center of gravity from the best fit sine wave for all slices as a grayscale image. We have ignored slices (setting the error to 0) for which a meaningful measurement of the center of gravity cannot be made. This includes slices for which the total absorption is very small (e.g. only air) or very large (complete absorption). One can clearly see that there are certain projection angles with consistently positive errors

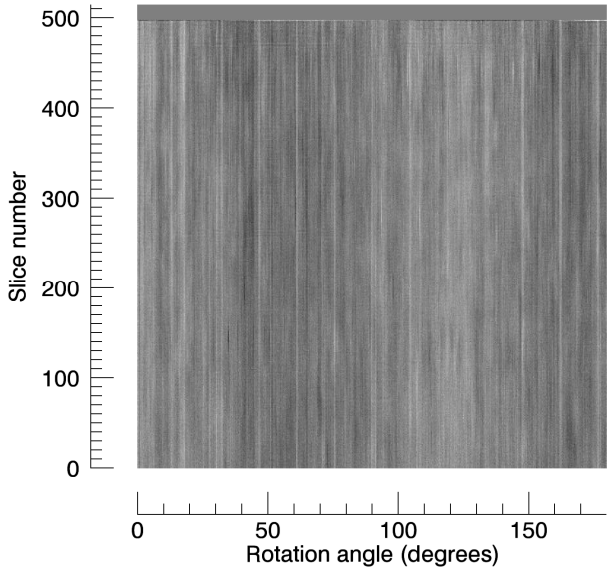

Figure 14. Deviation of center-of-gravity of sinogram from best-fit sine function for all slices. Bright is positive error, dark is negative error.

from the fit, and others with consistently negative errors.

Figure 15 shows the average deviation in pixels from the best-fit sine as a function of projection angle for all valid (non-air) slices in this dataset. Also shown is the nearest integer value to the average. This integer value is the amount that that projection was shifted horizontally to correct for the computed error in the rotation stage. Each projection was thus shifted by -1, 0, 1, or 2 pixels to produce the corrected sinogram shown in Figure 16. Figure 16B has a much smoother profile than Figure 11B, demonstrating

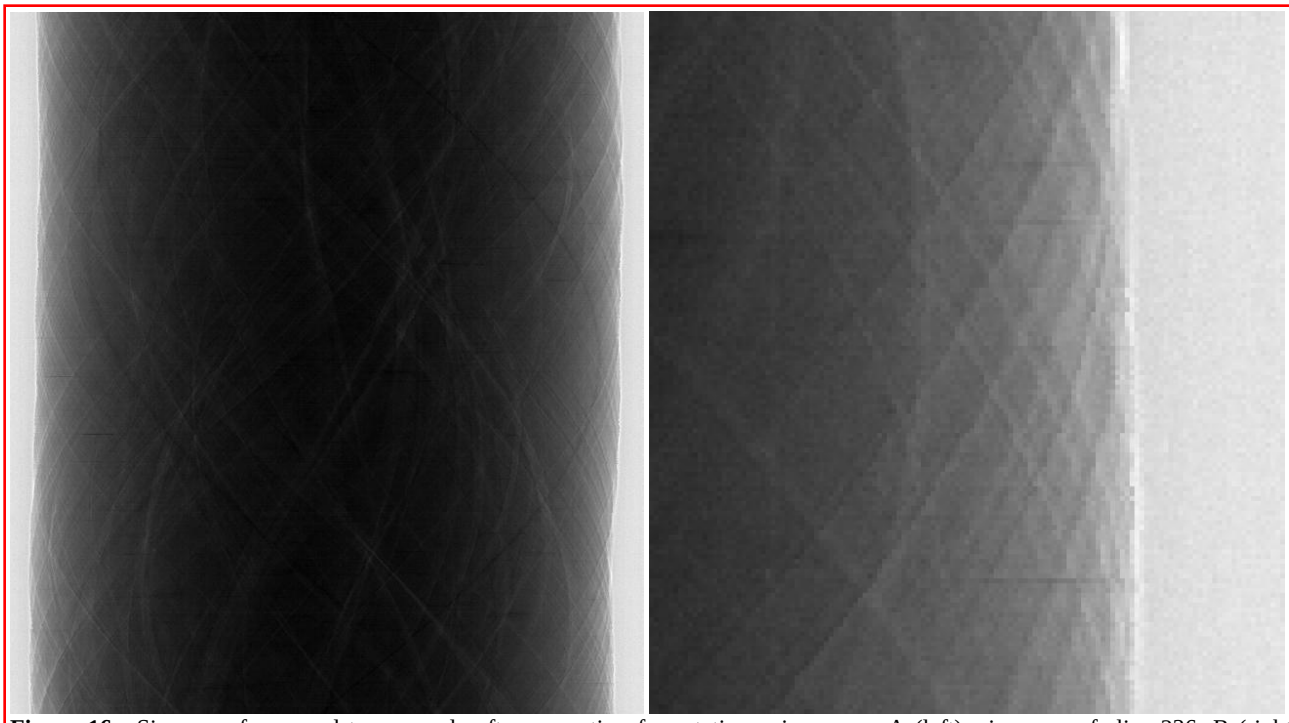

Figure 16. Sinogram from sandstone sample after correction for rotation axis errors. A (left): sinogram of slice 236; B (right): enlargement of lower right part of sinogram. Note the ragged edges seen in Figure 11 have largely disappeared.

that the center-of-gravity technique is successful in determining and correction the errors in the rotation stage.

Figure 17 compares reconstructed slices using the original sinogram in Figure 11, and using the corrected sinogram in Figure 16. Note that there are significantly fewer streaks in the reconstruction after correction, and that bright objects are

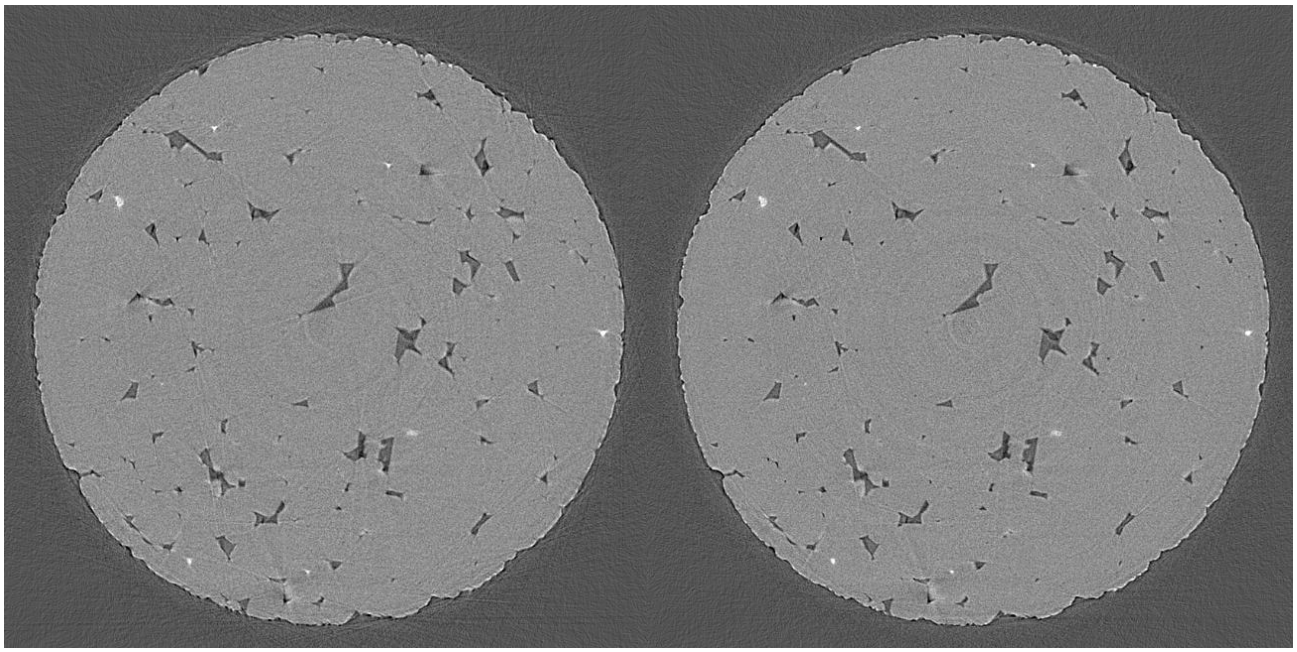

Figure 17. Reconstructed slices in sandstone. 20 keV, 650x650 slice, 3.36 µm pixels. A (left): before software correction of rotation axis errors; B (right): after correction of rotation axis errors. Image on right has fewer streaks and bright objects are better defined with fewer "tails".

better defined with much smaller wings or tails. Figure 18 is a similar comparison for a dataset on the same sample collected without binning, i.e. with 1.68x1.68 μm pixels. The effect of the correction is even more dramatic, with a very significant reduction in the streaks in the image. The rotation center correction both reduces the noise and improves the resolution.

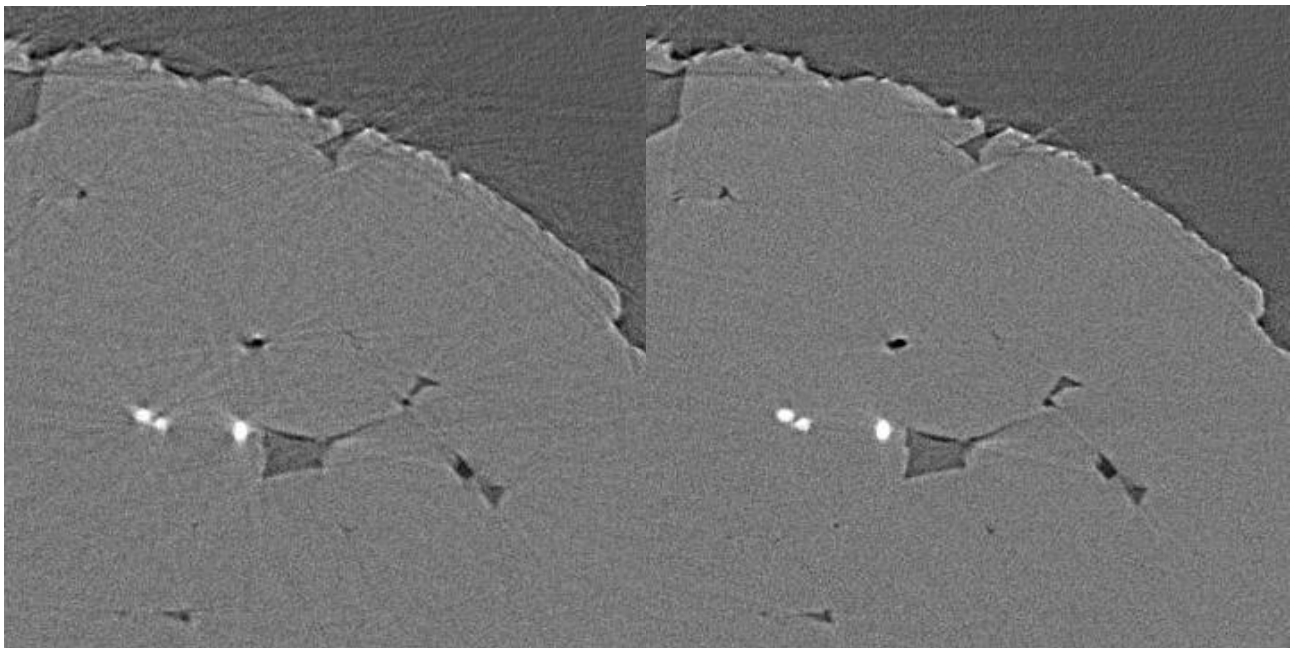

Figure 18. Enlarged view of reconstructed slices in sandstone. 20keV, 1300x1300 slice, 1.68 μm pixels. A (left): before software correction of rotation axis errors; B (right): after correction of rotation axis errors. Image on right has fewer streaks, less noise, and better resolution.

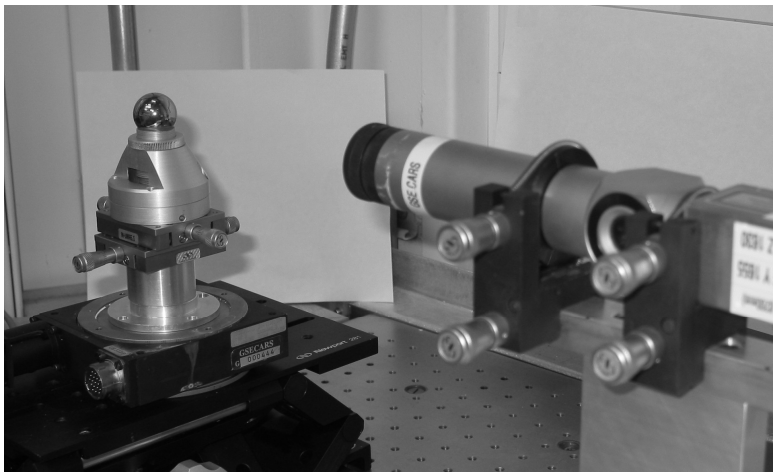

Figure 19. Photograph of a Newport LAE500 laser autocollimator. This device was used to measure the horizontal and vertical motion of the precision reflective ball mounted near the rotation axis of the rotation stage under test.

In order to characterize the performance of our rotation stages we made measurements with a Newport LAE500 laser autocollimator. This device is shown in Figure 19. The autocollimator works by measuring the difference in angle between a highly collimated outgoing plane wave and the returning wave reflected from a mirror. When used with a plane mirror the device is useful for determining, for example, the straightness of travel of a linear translation stage. For these measurements we used the autocollimator with a 200mm focal length lens and a precision reflective steel ball mounted near the rotation center of the rotation stage under test (Figure 19). In this configuration the autocollimator measures the horizontal and vertical position of the ball with a precision of 0.1 μm. We rotated the stage 360° while measuring the ball position. There is an expected sinusoidal motion in both directions if the ball is not mounted exactly on the rotation axis of the stage. We fitted the data to remove the sinusoidal component and then analyzed the residual position errors.

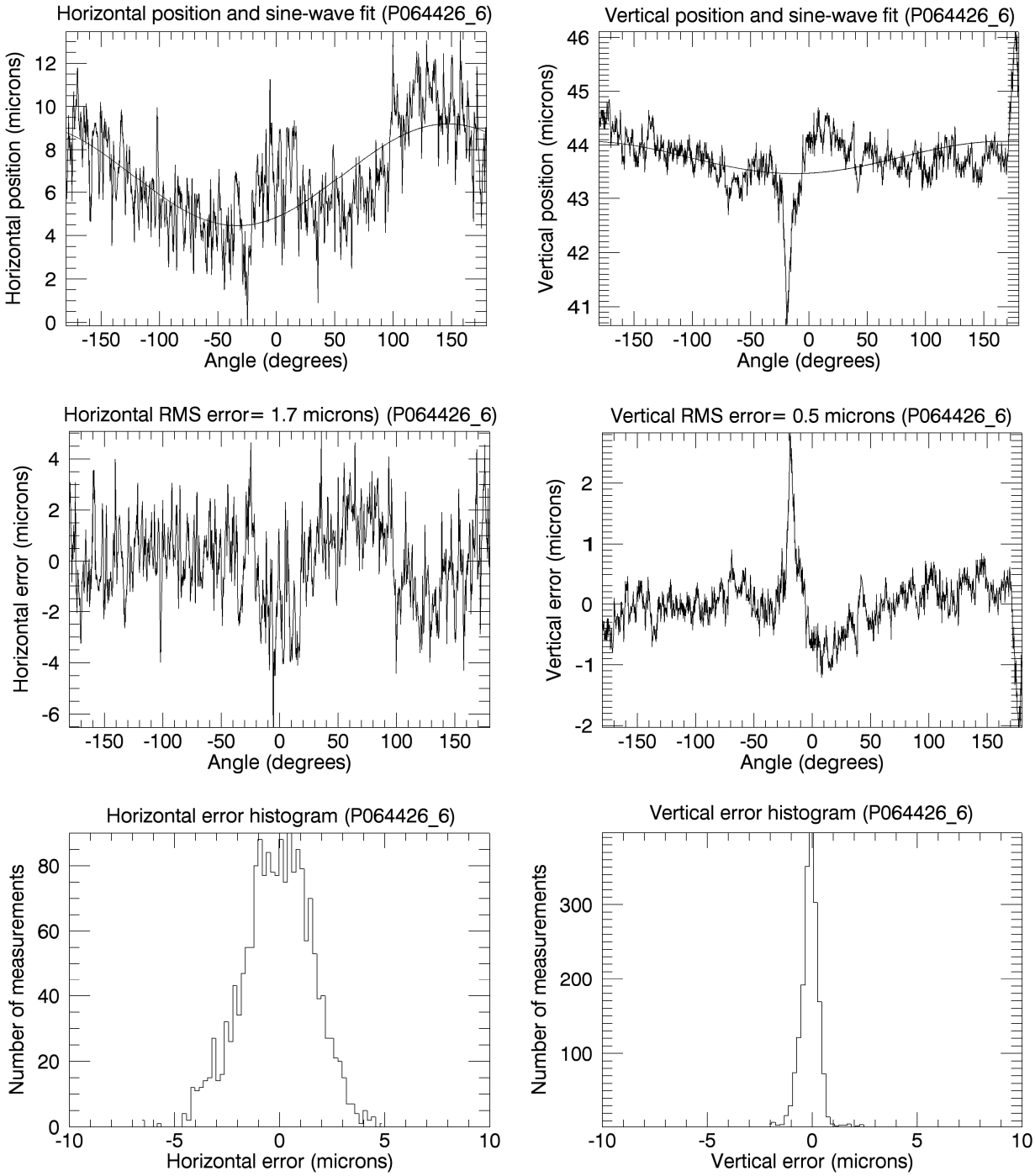

Figure 20. Autocollimator measurements of the horizontal and vertical motion of a high quality ball mounted close to the rotation axis of Newport URM80 rotation stage P064426. Top: horizontal and vertical position, and best-fit sine wave. Center: The difference of the measured position and the best-fit sine wave. Bottom: Histogram of errors, bin size = 0.2 µm. The RMS error in the horizontal is 1.7 µm, with a significant number of angles having errors as large as 4 µm. This is the stage that was used for microtomography at GSECARS until July 29, 2006.

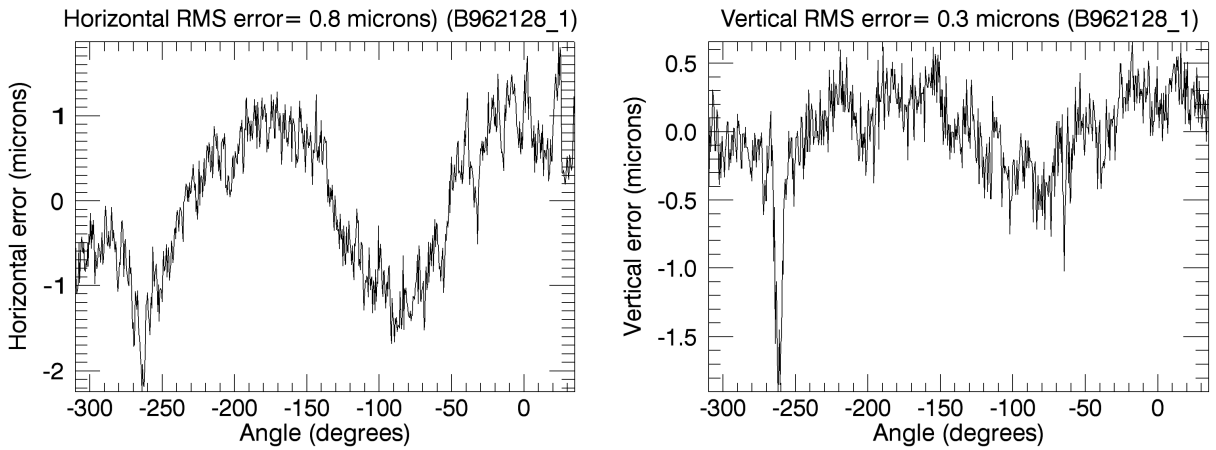

Figure 21. Autocollimator measurements of the horizontal (A, left) and vertical (B, right) motion of a high quality ball mounted close to the rotation axis of Newport URM80 rotation stage B962128. The difference of the measured position and the best-fit sine wave The RMS error in the horizontal is 0.8 µm. This is the stage that was used for microtomography at GSECARS starting July 29, 2006.

Figure 20 shows the autocollimator measurements for the rotation stage that was in use on our tomography system for several years, until it was replaced in late July 2006. The RMS deviation from a best-fit sine wave is 1.7 µm in the horizontal direction. There are many deviations as large as ±4 µm, and these are largely periodic, indicating a correlation with the position of the worm gear or the bearings. The vertical RMS error is 0.5 µm, and we have established that the large (2-3 µm) deviations at -20° and 180° are due to imperfections in the ball, not errors in the stage. These measurements confirm the significant horizontal errors that we saw in the microtomography data, with the same periodicity that we observed in the sinograms.

Figure 21 shows the autocollimator measurements on another Newport URM80 stage that we have used to replace the stage we had previously used. This stage has an RMS error of 0.8 µm in the horizontal direction and 0.3 µm in the vertical. If we ignore the one spike due to the imperfection in the ball at -260° then nearly all horizontal measurements are within ±1 µm of the best-fit sine wave.

The conclusion is that the laser autocollimator provides an excellent tool to characterize the rotation stages, and that the algorithm we have presented does a good job of correction rotation stage errors when they are present.

4. NEW TECHNIQUES

4.1 High Pressure Tomography

One of the most recent, and exciting developments at GSECARS is the capability to perform microtomography experiments at high pressure, up to 10 GPa. The apparatus consists of a 250-ton press, which is normally used for high-pressure diffraction experiments at GSECARS at 13-BM-D. Inside the press is a special tooling called a Rotational Drickamer cell that uses thrust bearings to allow rotation while under loads of up to 50 tons. This design is based on a deformation apparatus designed by Yamazaki and Karato[14]. The design parameters of this system include[15]: maximum load capacity of 50 T; rotation range of 360° with 0.02° repeatability; lateral translation of apparatus by ~ 50 mm, repeatable within 2 µm; maximum pressure of 10GPa, maximum temperature of 1500K; sample size of 1 mm diameter, 0.5 mm long; monochromatic diffraction and imaging a spatial imaging resolution of ~2 µm (Figure 21). The modes of operation involve rotating the anvils in-phase for high-P tomography, and rotating the anvils out-of-phase for shear deformation. Using this device in its high-P tomography mode we plan to study: in-situ observations of phase separation, including melts; the effects of deformation on melt texture and evolution; the density of melts and liquids through measurements of the x-ray linear attenuation coefficient. We have used the 3-D imaging capabilities to make volume measurements of glasses, and plan to extend this to liquids and melts with no assumptions about sample geometry at high-P.

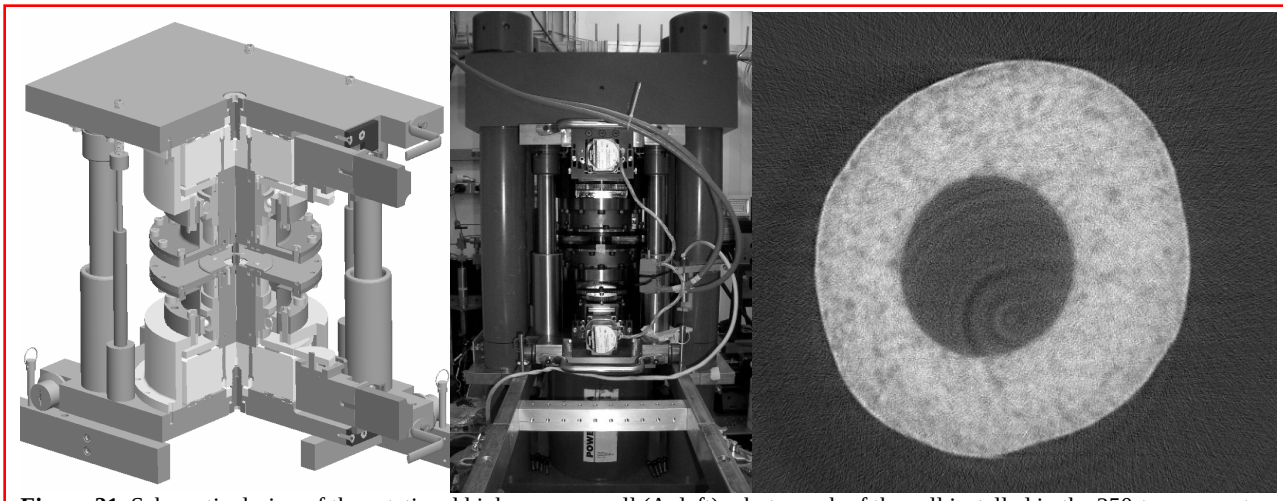

Figure 21. Schematic design of the rotational high-pressure cell (A, left); photograph of the cell installed in the 250-ton press at GSECARS 13-BM-D (B, center); reconstructed slice from one of our first data sets (C, right). This slice was collected at 45 keV with 6 μm pixels. The sample is Fe-9%S with a sapphire sphere in the center. The load was 12 tons and the pressure about 4GPa.

4.2 High Speed Radiography

We have recently used the 13-BM-D station to perform very high speed radiography experiments, imaging the dynamics when a steel ball is dropped into a bed of granular material[3]. The data were collected using a pink beam, i.e. white beam with a high energy cutoff set to ~25 keV by the use of the vertical focusing mirror, and the low energy cutoff set to ~15 keV by placing aluminum absorbers in the beam. The vertical mirror was also used to defocus the beam, to achieve a vertical beam height of ~10mm. We used a Phantom CMOS camera to record 8-bit images (800x600 pixels) with frame rates of 5,000 frames/s and exposure times of 100 μs.

5. ACCESS

Access to the GSECARS CMT facility is available to the community, with preference given to earth-science related research. Information can be obtained at http://www.gsecars.org, and application for beam time at http://www.aps.anl.gov. The absorption CT apparatus currently runs on the bending magnet beamline approximately 25% of the time, and fluorescence CT is run on the undulator beamline in conjunction with the XRF microprobe.

6. FUTURE PLANS

The GSECARS CMT system has undergone continuing upgrades and enhancements over the years. The following enhancements to the facility are planned for the near future:

- Rebuild the camera mount to allow direct viewing of scintillator by objective lens, without a mirror. This will permit use of high numerical aperture lenses for higher resolution.
- Support new CCD cameras. We have ordered CoolSNAP K4 (2048x2049 pixels, 20MHz) and CoolSNAP HQ2 (1394x1040 pixels, 20MHz) cameras from Photometrics. These cameras are four times faster than our existing system with larger full-well depths and lower read noise.
- Rewrite the data collection software in IDL, converting from Visual Basic. This will make it easy to add features like autofocusing using IDL's image processing capabilities..
- Add automated optimization of the rotation center location during reconstruction. Allow sub-pixel rotation centers, and rotation centers which vary linearly with slice number, for cases where the alignment of the rotation stage and CCD columns is not perfect.
- Add functions to automatically register volumes when doing differential absorption tomography, for the cases when the sample has moved slightly between energies.
- Use of better scintillators to reduce the spatial resolution to below 1 μm when required.

7. ACKNOWLEDGEMENTS

GSECARS is supported by the National Science Foundation Earth Sciences Instrumentation and Facilities Program, the Department of Energy Engineering and Geosciences Program, the W.M. Keck Foundation, and the State of Illinois

Board of Higher Education. The projects described in this paper were done in a collaboration with a large number of external users of the GSECARS facilities. We would like to thank the following people for use of data in this paper: Denton Ebel, Francesco De Carlo, Joanne Fredrich, Don Baker, Charles Lesher, and John Royer.

8. REFERENCES

1. M.L. Rivers, S.R. Sutton, and P. Eng "Geoscience applications of x-ray computed microtomography", Proceedings of SPIE, *Developments in X-Ray Tomography II*, **3772**, 78-86, 1999.
2. M.L. Rivers, Y. Wang, and T. Uchida "Microtomography at GSECARS", Proceedings of SPIE, *Developments in X-Ray Tomography IV*, **5535**, 783-791, 2004.
3. J.R. Royer, E.I. Corwin, A. Flior, M.L. Cordero, M. Rivers, P. Eng, and H.M. Jaeger, "Formation of granular jets observed by high-speed x-ray radiography" Nature Phys. **1**, 164-167, 2005.
4. G. Schnaar, M.L. Brusseau, "Characterizing Pore-Scale Configuration of Organic Immiscible Liquid in Multiphase Systems With Synchrotron X-Ray Microtomography", Vadose Zone J. **5**, 641-648, 2006.
5. R.I. Al-Raoush, C.S. Willson, "A Pore-scale Investigation of a Multiphase Porous Media System", J. Contam. Hydrol. 77, 67-89, 2005.
6. K.A. Culligan, D. Wildenschild, B.S.B. Christensen, W.G. Gray, M.L. Rivers, "Pore-scale Characteristics of Multiphase Flow in Porous Media: a Synchrotron-based CMT Comparison of Air-Water and Oil-Water Experiments", Adv. Water Resour. **29**, 227-238, 2006.
7. B. Dowd, G.H. Campbell, R.B. Marr, V. Nagarkar, S. Tipnis, L. Axe, D.P. Siddons "Developments in synchrotron x-ray computed tomography at the National Synchrotron Light Source" Proceedings of SPIE, *Developments in X-Ray Tomography II*, **3772**, 224-236, 1999.
8. M. Frigo and S. G. Johnson, "The Design and Implementation of FFTW3", Proceedings of the IEEE **93**, 216–231, 2005.
9. R.A. Ketcham "Computational methods for quantitative analysis of three-dimensional features in geological specimens" Geosphere: **1**, 32–41, 2005
10. W. B. Lindquist and A. Venkatarangan "Investigating 3D geometry of porous media from high resolution images" Phys. Chem. Earth (A), **25**, 593-599, 1999
11. G.R. Davis, and J.C. Elliot, "X-ray microtomography scanner using time-delay integration for elimination of ring artifacts in the reconstructed image", Nucl. Instr. Meth. Phys. Res. A, **394**, 157-162, 1997.
12. R.A. Ketcham "New algorithms for ring artifact removal", Proceedings of SPIE, *Developments in X-Ray Tomography V*, **6318**, 2006 (this volume).
13. S. W. Wilkins, S. C. Mayo, P. R. Miller, T. E. Gureyev, A. W. Stevenson, D. Gao, D. M. Paganin, "Quantitative submicron phase-contrast CT using an SEM-based full-field x-ray microscope", Proceedings of SPIE, *Developments in X-Ray Tomography V*, **6318**, 2006 (this volume).
14. D. Yamazaki and S. Karato, High pressure rotational deformation apparatus to 15 GPa, Rev. of Sci. Instrum., **72,** 4207-4211, 2001.
15. Y. Wang, T. Uchida, F. Westferro, M.L. Rivers, J. Gebhardt, C.E. Lesher, S.R. Sutton, "High-Pressure X-ray Tomography Microscope: Synchrotron Computed Microtomography at High Pressure and Temperature", Rev. Sci. Instrum. **76**, 073709-1-073709-7, 2005.